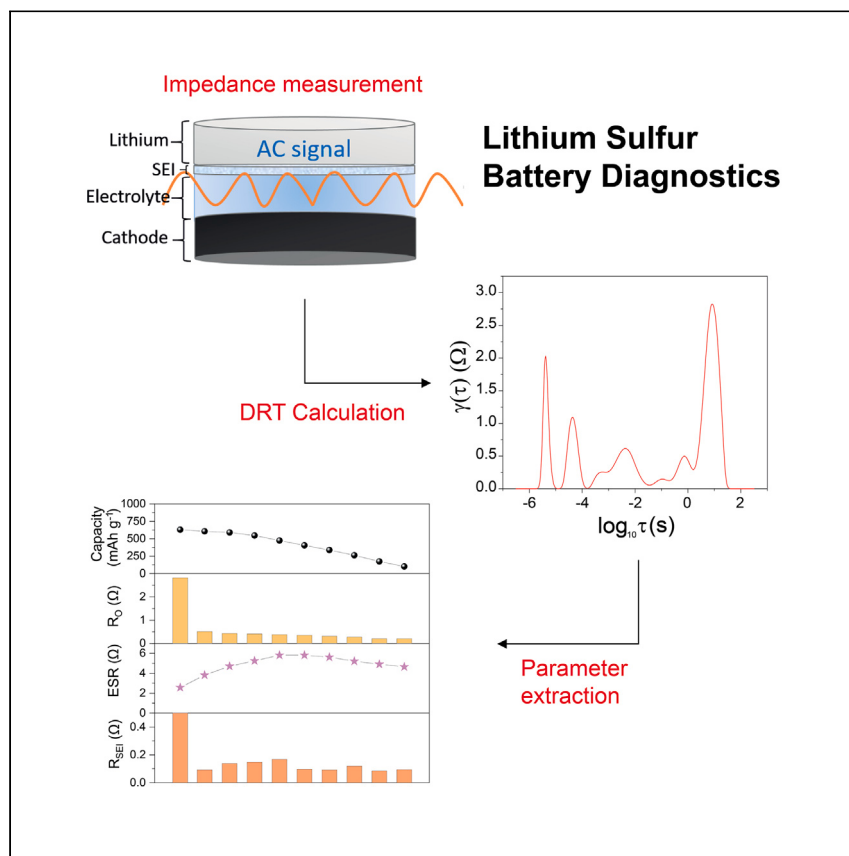


**Article**

# Predicting cell failure and performance decline in lithium-sulfur batteries using distribution of relaxation times analysis



Soni et al. demonstrate the application of the distribution of relaxation times method as a diagnostic tool for the analysis and prediction of capacity fade and end-of-life of Li-S batteries. The instability of the SEI and the high rate of  $\text{Li}_2\text{S}$  precipitation are shown to be primary indicators of performance loss.

Roby Soni, Ji Hu, James B. Robinson, Alexander J.E. Rettie, Thomas S. Miller

t.miller@ucl.ac.uk (T.S.M.)

## Highlights

Li-S battery solid electrolyte interphase resistance ( $R_{SEI}$ ) is linked to cell health

Abrupt reduction in the  $R_{SEI}$  is associated with decline in cell health and failure

Soft-shorts can be identified and characterized via the reduction in impedance and  $R_{SEI}$

Past 'end-of-life' (80% initial capacity) capacity fade is linked to  $\text{Li}_2\text{S}$  precipitation



Article

# Predicting cell failure and performance decline in lithium-sulfur batteries using distribution of relaxation times analysis

Roby Soni,<sup>1,2</sup> Ji Hu,<sup>1,2</sup> James B. Robinson,<sup>1,2</sup> Alexander J.E. Rettie,<sup>1,2,\*</sup> and Thomas S. Miller<sup>1,2,3,\*</sup>

## SUMMARY

While lithium-sulfur (Li-S) batteries are a promising next-generation technology, their complex chemistry means they can degrade and fail via numerous mechanisms. To minimize or overcome these modes of failure, we must develop tools that can differentiate between chemical processes in the operating cell, reveal their effects on cell health, and monitor cells throughout their lifetimes. In this study we undertake a comprehensive investigation of the failure modes exhibited by Li-S cells, using the distribution of relaxation times (DRT) method. By evaluating the contribution of various electrochemical processes to overall cell resistance, we establish meaningful correlations between performance degradation and specific electrochemical/materials phenomena. Notably, the DRT profiles reveal that the solid-electrolyte interphase resistance can serve as an early indicator of impending cell failure. The methodologies and findings presented in this study hold substantial implications for the advancement of on-board diagnostics tailored for Li-S batteries and other cell chemistries.

## INTRODUCTION

Despite the promise of lithium-sulfur (Li-S) batteries (i.e., high energy density, low cost, and comparative safety), their complex modes of cell degradation and tendency for premature failure still hinder their commercial application. More importantly, although Li-S batteries can reach capacities close to their theoretical values ( $1,675 \text{ mAh g}^{-1}$ )<sup>1</sup> in initial cycles, these usually decline rapidly due to factors including polysulfide (PS) shuttling,<sup>2</sup> cracking of positive and negative electrodes, increases in interfacial resistance, and electrolyte loss due to the continuous formation of solid electrolyte interphase (SEI). Unfortunately, although the use of tools to understand the state-of-health (SoH) of Li-S batteries will be vital for their commercial success, the complexity of the Li-S system means that the use of more generalized or widely used SoH estimation methods will be very challenging, even after the usual customization to tailor for a specific cell chemistry.<sup>3</sup> SoH estimation methods currently used for Pb acid, Li-ion, and metal hydride batteries are commonly based on various capacity or impedance measurements and the correlation of these data with known battery phenomena.<sup>4–6</sup> The application of these simple methods of analysis are, however, unreliable for Li-S batteries due to peculiarities in the cell behavior, such as a tendency toward high-self discharge, variable length and shape of the charge-discharge curves, and the fluctuations in open-circuit voltage (OCV).<sup>7</sup> Therefore, battery health estimation methods that show a strong and direct correlation with variations in the Li-S battery chemistry and features are required for their diagnosis.

Recent investigations have demonstrated that the distribution of relaxation times (DRT) analysis of electrochemical impedance spectroscopy (EIS) data is an effective *in situ*

<sup>1</sup>Department of Chemical Engineering, Electrochemical Innovation Lab, University College London, London WC1E 7JE, UK

<sup>2</sup>The Faraday Institution, Quad One, Harwell Science and Innovation Campus, Didcot OX11 0RA, UK

<sup>3</sup>Lead contact

\*Correspondence: [t.miller@ucl.ac.uk](mailto:t.miller@ucl.ac.uk) (T.S.M.), [a.rettie@ucl.ac.uk](mailto:a.rettie@ucl.ac.uk) (A.J.E.R.)

<https://doi.org/10.1016/j.xcpr.2024.101833>



diagnosis tool for understanding Li-S battery formation and early-cycle life loss processes.<sup>8,9</sup> It was shown to be able to distinguish between a wide range of simultaneously occurring modes of capacity loss, and to enable the analysis of cell state-of-charge (SoC). Here, we apply this tool to reveal the processes that drive Li-S battery degradation, SoH, and failure.

Although several studies have been undertaken to date to decipher the mechanisms of performance change during Li-S battery cycling, there are still inconsistencies in findings and, more importantly, few studies identify methods that could be used to predict instances of cell degradation or failure. For example, in their capacity fade analysis for Li-S cells using EIS, Noh et al. linked improvements in capacity retention at high discharge currents to the formation of amorphous  $\text{Li}_2\text{S}$  at the positive electrode, which led to faster Li-ion diffusion. This in turn led to low overpotentials and high reversibility compared to crystalline  $\text{Li}_2\text{S}$ , which formed at low discharge currents.<sup>10</sup> Yan et al. also linked capacity fade to  $\text{Li}_2\text{S}_2/\text{Li}_2\text{S}$  films forming on the S positive electrode, via postmortem scanning electron microscopy analysis, combined with EIS. In tests with different amounts of electrolytes over 100 charge-discharge cycles, the cell with  $12 \mu\text{L}/\text{mg}_{\text{Sulfur}}$  electrolyte lost 61% capacity, whereas the cell with  $5 \mu\text{L}/\text{mg}_{\text{Sulfur}}$  electrolyte lost 30% capacity after 100 cycles.<sup>11</sup> However, this study did not analyze the negative electrode for its role in capacity fade. This is important because Risse et al. found a contribution from the negative electrode toward early-cycle life ( $\sim 50$  cycles) capacity fade processes in the Li-S cell in an early study combining EIS with DRT analysis.<sup>12</sup> In particular, they identified a fast capacity loss process in the initial cycles and low fade process in later cycles using a linear four-state model. The slowing of charge transfer at the negative electrode was found to primarily contribute to the fast degradation, whereas the deposition of  $\text{Li}_2\text{S}$  in later cycles was responsible for the slower degradation process. More widely, capacity losses have been strongly linked to the PS shuttle effect, including irreversible processes leading to PS oxidation at the negative electrode and quasireversible capacity losses attributed to the PS dissolution in electrolytes, which can be recovered on slow charging.<sup>13</sup>

Here, we demonstrate that DRT analysis of EIS can be used to characterize the multi-faceted processes that drive Li-S battery degradation throughout cell life, from early-cycle capacity losses to midlife plateaus and end-of-life drop-off. The understanding of the Li-S battery characteristics developed enable a deeper understanding of Li-S battery chemistry and offer a powerful predictive tool to identify cell SoH and even cell failure. This is achieved using *in situ* methods that are relevant to onboard battery management systems, and hence the knowledge gained can significantly contribute to future Li-S battery efficiency, control, and safety.

## RESULTS AND DISCUSSION

### Capacity fade analysis during end-of-life operation

Previous work<sup>8</sup> identified eight distinct relaxation time constants for Li-S cells, in which peak P1 (see Figure S1;  $\sim 3 \mu\text{s}$ ) was assigned to distributed Ohmic resistance ( $R_O$ ), P2 ( $14\text{--}28 \mu\text{s}$ ) to double-layer relaxation, P3 ( $\sim 45 \mu\text{s}$ ) to Li-ion migration through the SEI at the negative electrode ( $R_{SEI}$ ), P4–P6 ( $\sim 0.3, 0.5$ , and  $50 \text{ ms}$ ), respectively, to the charge-transfer resistance at the positive electrode, and P7 and P8 ( $\sim 0.4$  and  $10 \text{ s}$ ) to diffusion processes. The resistance contribution of the above parameters to the total cell resistance can be quantified by calculating the area under these peaks, which can be correlated to processes contributing to the performance loss.<sup>14</sup> To decipher modes of capacity loss toward the end-of-life of Li-S cells (end-of-life is defined here as the loss of 20% of the initial capacity during cycling) at low current densities (C/20), we performed DRT measurements after 5 charge-discharge cycles (at 100% SoC) until the cell reached  $\sim 80\%$  of

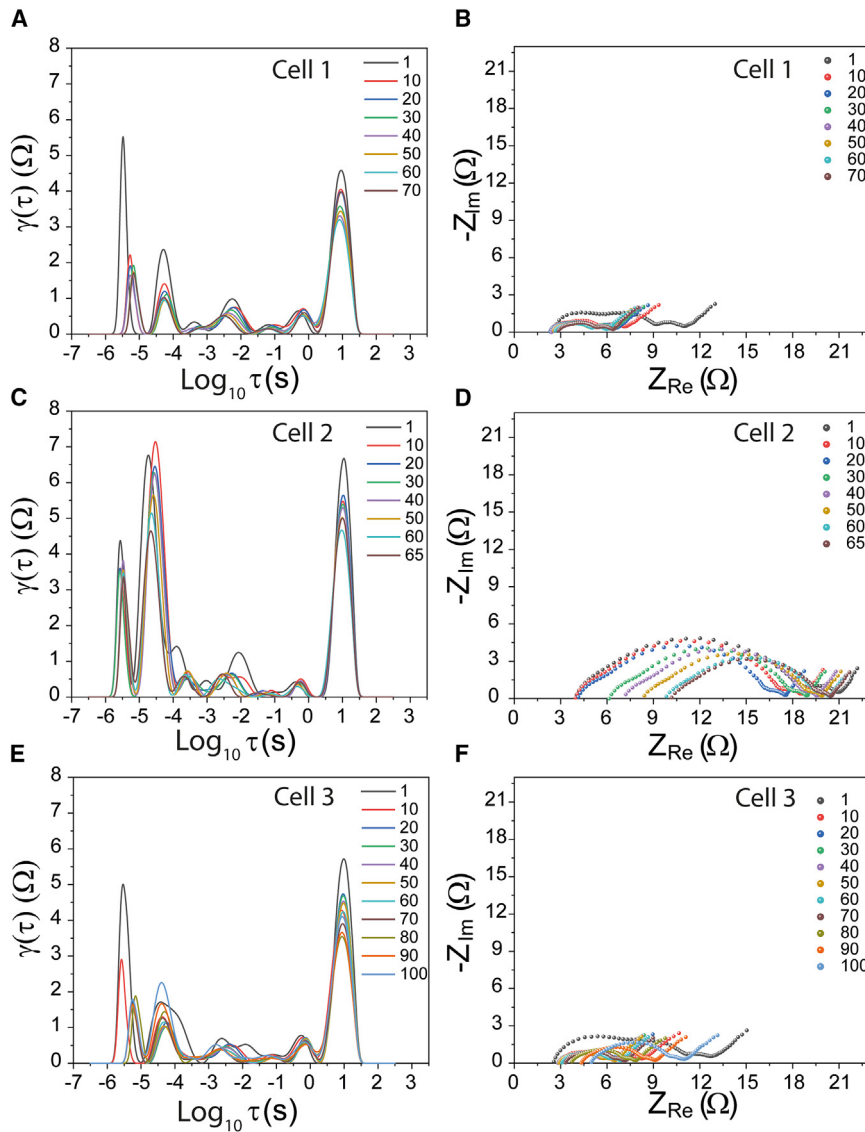


**Figure 1. Impedance data and DRT analysis**

DRT profiles (A, C, and E) and the corresponding impedance data (B, D, and F) recorded every 10 cycles at 100% SoC as the cell is cycled at C/20 current density until the cells reach end-of-life (80% capacity).

the initial capacity<sup>15</sup> on cells fabricated with lab-made electrodes (see [Experimental procedures](#)). **Figure 1** shows the evolution of the impedance data and DRT profile (time constants and polarization resistance) measured after every 10 charge-discharge cycles (every 5 charge-discharge cycles are shown in [Figure S2](#)) for 3 representative cells until they reached end-of-life. DRT profiles ([Figures 1A, 1C, and 1E](#)) and the corresponding Nyquist plots ([Figures 1B, 1D, and 1F](#)) exhibit continuous change with cycling, indicating changes in the properties of the positive electrode, negative electrode, electrolyte, and electrochemical interface; the observed DRT profiles are consistent with those reported previously.<sup>8</sup>

In [Figure 2](#), the evolution of several key resistance components is quantified from the DRT profiles for cells 1, 2, and 3 as they reached end-of-life, plotted alongside the

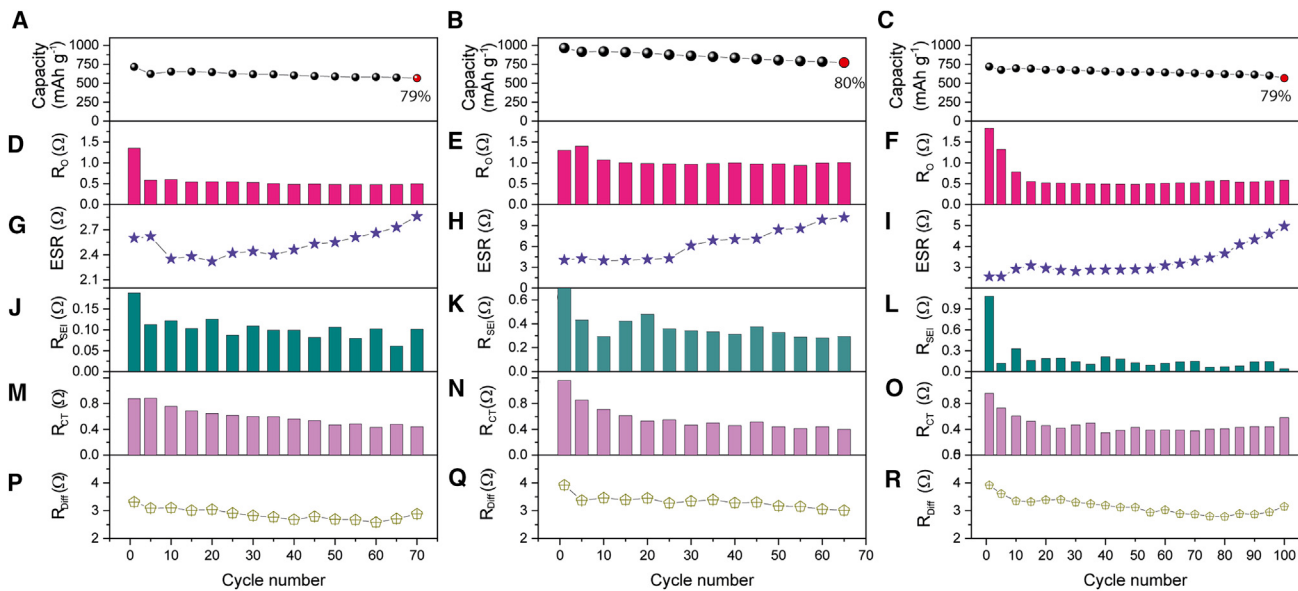


**Figure 2. Resistance contribution of different cell processes**

The trend in resistance contribution of different cell processes in lab-made cells extracted from DRT profiles at C/20.

(A–C) Capacity values measured for cells 1, 2, and 3 at C/20 through end-of-life.

(D–F)  $R_O$  values.

(G–I) ESR values.

(J–L)  $R_{SEI}$  values.

(M–O)  $R_{CT}$  values.

(P–R)  $R_{Diff}$  values.

See Tables S1, S2, and S3 for values.

cell capacity as a function of cycle number. The initial discharge capacities measured for cells 1, 2, and 3 (after the formation cycle in which cell capacities were 715, 965, and 719 mAh g<sup>-1</sup>, respectively, which decreased to 623, 915, and 675 mAh g<sup>-1</sup> after 5 cycles, a loss of 12.8%, 5.2%, and 6.1%, respectively; Figures 2A–2C). Upon further cycling, the cell capacity fades steadily, eventually reaching end-of-life after 70, 65, and 100 cycles, respectively, for the 3 cells; a similar capacity loss during cycling has been observed in the literature.<sup>11,16–19</sup>  $R_O$  (P1, Figures 2D–2F), the interparticle resistance, decreases in the initial stage of cycling in all of the cells, which is attributed to the rearrangement of S and remains largely consistent, with only minor fluctuations toward end-of-life; it can be excluded as a major driver of the performance change observed because no correlation with degradation events was observed.

It is interesting that the equivalent series resistance (ESR) (Figures 2G–2I) of the cells, to which the electrolyte resistance makes the major contribution, did not increase abruptly in the initial cycles but instead could be seen to increase slowly in the middle of cycle life and at a faster rate afterward. For example, in cell 1 (Figure 2G), after an initial increase from the precycling value to that measured in cycle 1 (2.40–2.60 Ω), the ESR remained steady between the first to the fifth cycle, exhibiting a nominal change from 2.60 to 2.62 Ω. An increase in electrolyte viscosity will act to increase ESR, suggesting that in the early cycles, the reduction in any PSs, which significantly increase electrolyte viscosity, back to Li<sub>2</sub>S within the positive electrode or on the Li surface prevents any major increase in electrolyte viscosity.<sup>2</sup> As the cycling progresses, the ESR experiences a gradual but consistent increase, culminating in end-of-life scenarios in which electrolytes saturated with PSs will certainly play a role. For example, in cell 2 (Figure 2H), the ESR displays a slight increase during

the first 25 cycles, ranging from 4.03 to 4.26  $\Omega$ , followed by a steady increase to 10.17  $\Omega$  after cycle 65. This behavior is mirrored in cells 1 and 3 (Figures 2G and 2I).

An analysis of the resistance of SEI ( $R_{SEI}$ ), as illustrated in Figures 2J–2L, reveals a discernible reduction in resistance during the early cycles while the interphasial layer is forming for all cells, indicative of inherent instability and reactivity within the SEI. However,  $R_{SEI}$  then undergoes continuous and uneven changes, indicating the unstable nature of the Li surface; notably, the  $R_{SEI}$  does not manifest any discernible trend across all of the cells, underscoring the highly dynamic nature of the interphase due to the continual stripping and plating of Li during discharge and charge cycles. The inherent instability of the SEI exposes fresh Li after each cycle, contributing to electrolyte degradation and PS reduction, and thereby contributing to the observed capacity decay.<sup>20</sup> These data show that these events occur concurrently with major changes in the cell capacity behavior; therefore, the instability of the SEI, when the Li-S cell is operated at C/20, is likely a major contributor to the capacity decay.

Unlike  $R_{SEI}$ , the change in the double-layer polarization ( $R_{dl}$ ) at the positive electrode (Figure S3) shows little correlation to the observed phases of performance change. Changes in  $R_{dl}$  do not align with capacity fade and show fluctuations in the values as the cell is charge-discharged, indicating that the evolution of  $R_{dl}$  has little significance in the assessment of performance loss and cell diagnosis.

The higher time constants peaks, P4–P6, in the DRT analysis represent charge-transfer resistance ( $R_{CT}$ ) of the positive electrode (Figures 2M–2O), and it is interesting to note that these resistance values show a complicated behavior, fluctuating as the cells were cycled, but show an overall downward trend. Charge transfer at the positive electrode is influenced by the conductivity of the interface.<sup>21</sup> The absence of any uniform trend in the  $R_{CT}$  values indicates that the deposition of Li<sub>2</sub>S and S in the positive electrode following discharge and charge is also dynamic, hence the deposition is likely uneven and inconsistent when the cell is operated at C/20. Therefore, we find that the evolution of P4–P6 does not demonstrate an intimate correlation with capacity changes in the cell, suggesting their limited utility for the prediction of cell degradation and failure. Lastly, diffusion resistance ( $R_{Diff}$ ) (Figures 2P–2R, P7 and P8) is characteristic of ion-diffusion processes and is influenced by the porosity of the electrode structure and solid-state diffusion, showing an overall downward trend in cell 1, with a slight increase and decrease up to 60 cycles, followed by a linear increase toward end-of-life. In cells 2 and 3, the  $R_{Diff}$  values are slightly more stable, suggesting that Li<sub>2</sub>S precipitation is not a limiting process for the capacity fade at low current density (C/20) until cell end-of-life. The above analysis of different resistance contributions of the Li-S cell show that the instability of the SEI leading to PS reduction and electrolyte decomposition at the Li negative electrode are largely responsible for the capacity loss in Li-S cells at C/20.

### Capacity fade analysis toward cell death

Although understanding capacity fade toward the ‘end-of-life’ is important, the analysis and understanding of capacity degradation beyond this widely accepted, but arbitrarily defined, point as the cell moves towards true cell death is significant for second-life applications, particularly in high-energy-density systems such as Li-S batteries.<sup>22</sup> Hence, to enable the identification of failure mechanisms in Li-S batteries during long-term cycling toward cell death, and to detect precursors of cell failure, we monitored cells until their capacity became negligible, measuring EIS at 50 cycle intervals at 100% SoC to allow DRT analysis to be performed. Polarization resistances of various cell processes were quantified to determine the contributions of different cell polarizations toward cell failure.

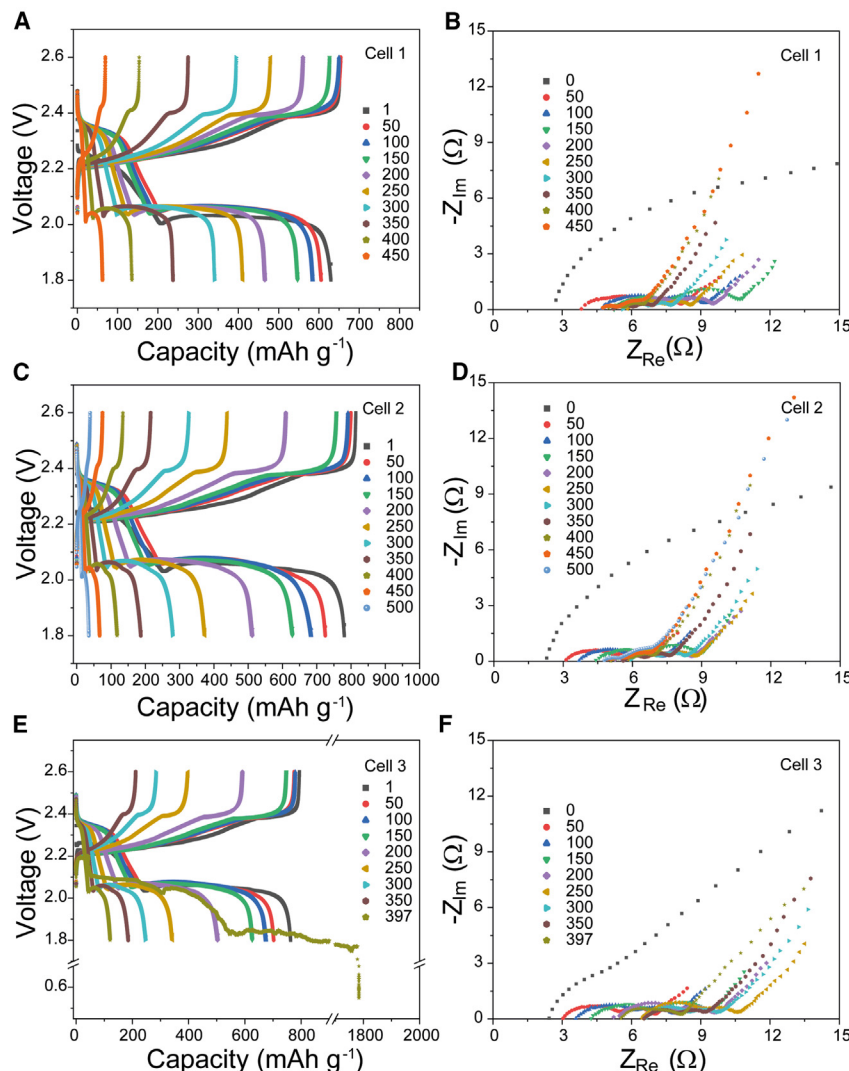


**Figure 3. Charge-discharge and impedance data**

Charge-discharge (C/5) and impedance data of cell 1 (A and B), cell 2 (C and D), and cell 3 (E and F) were measured at intervals of 50 cycles until cell capacity became negligible.

Cells fabricated with lab-made electrodes first underwent a formation cycle (discharge and charge) at a rate of C/20 (Figure S4; capacities obtained after the formation cycle, designated as 0 cycle, for cells 1, 2, and 3 were 885, 1,013, and 1,014 mAh g⁻¹, respectively), before they were subjected to long-term cycling at a rate of C/5. Charge-discharge curves and impedance data recorded at intervals of 50 cycles until cell capacity dropped to negligible are shown in Figure 3; cells 1, 2, and 3 show 630, 780, and 763 mAh g⁻¹ capacity after the first discharge, dropping to 504 (183 cycles), 624 (152 cycles), and 610 (160 cycles) at end-of-life. The capacity faded consistently in all 3 cells; the charge-discharge profiles show shrinking of the plateau between 2.4 and 2.0 V and 2.0 and 1.8 V, signifying the formation of PSs and indicating the loss of active material due to PS dissolution. Furthermore, the charge-discharge overpotential, measured at the midpoint voltage, gradually increased with cycling, ascribed to the increase in the internal resistance of the cell<sup>23</sup> ( $E = E_O - IR$ , where  $E$  is the cell voltage,  $E_O$  is the thermodynamic voltage,  $I$  is the current, and  $R$  is the resistance). Nyquist plots for 3 cells recorded after a

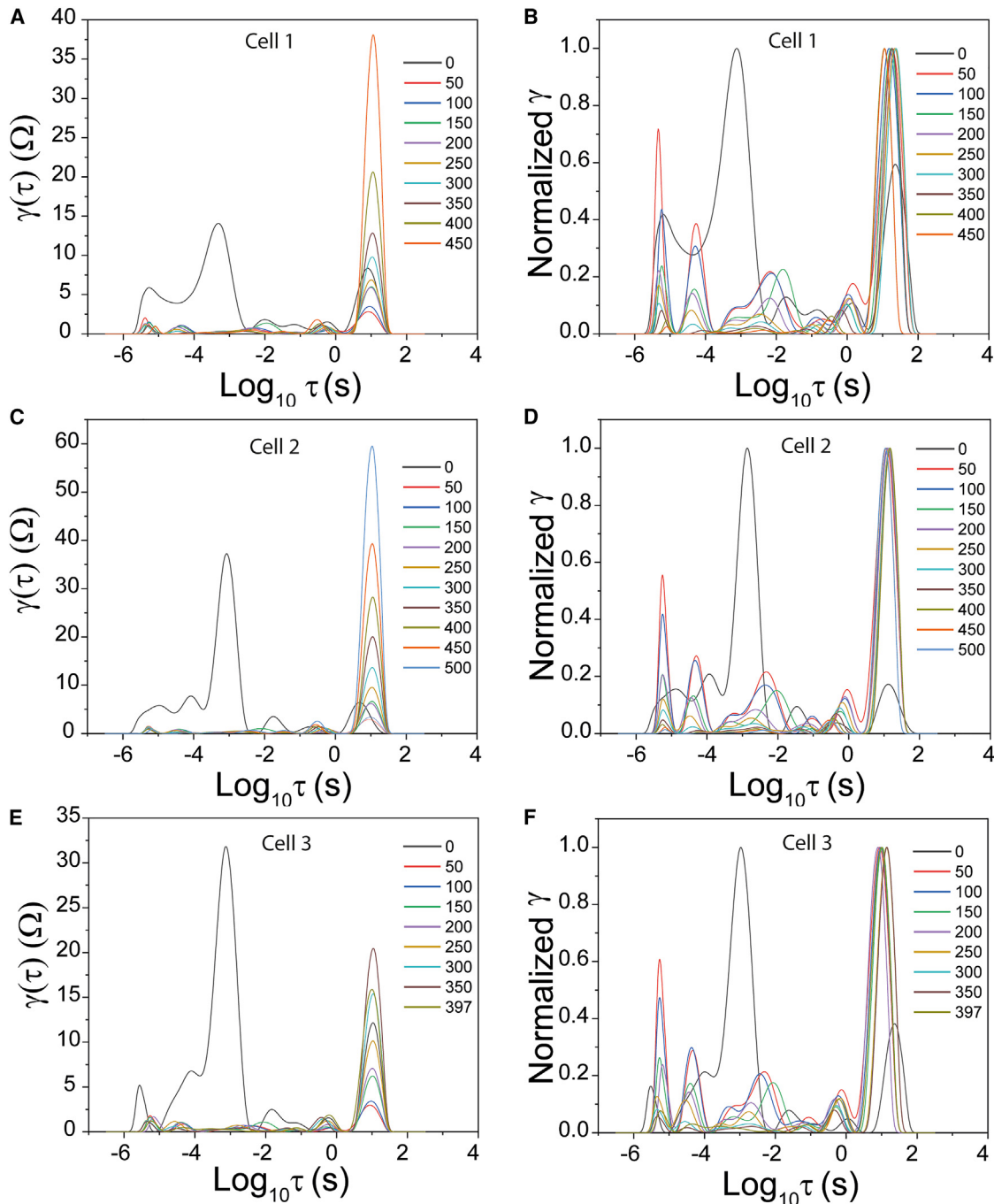


**Figure 4. DRT profiles and corresponding normalized DRT profiles**

DRT profiles (A, C, and E) and corresponding normalized DRT profiles (B, D, and F) of lab-made cells cycled at C/5.

consecutive 50 cycles are shown in Figure 3; the plots show that the EIS profile changes regularly as the cell is cycled, pointing toward the evolution of the internal properties of the cell, such as electrode structure, electrolyte resistance, and SEI.

DRT profiles calculated for the above three cells are shown in Figure 4; DRT profiles measured after the formation cycle show very high resistance for the negative

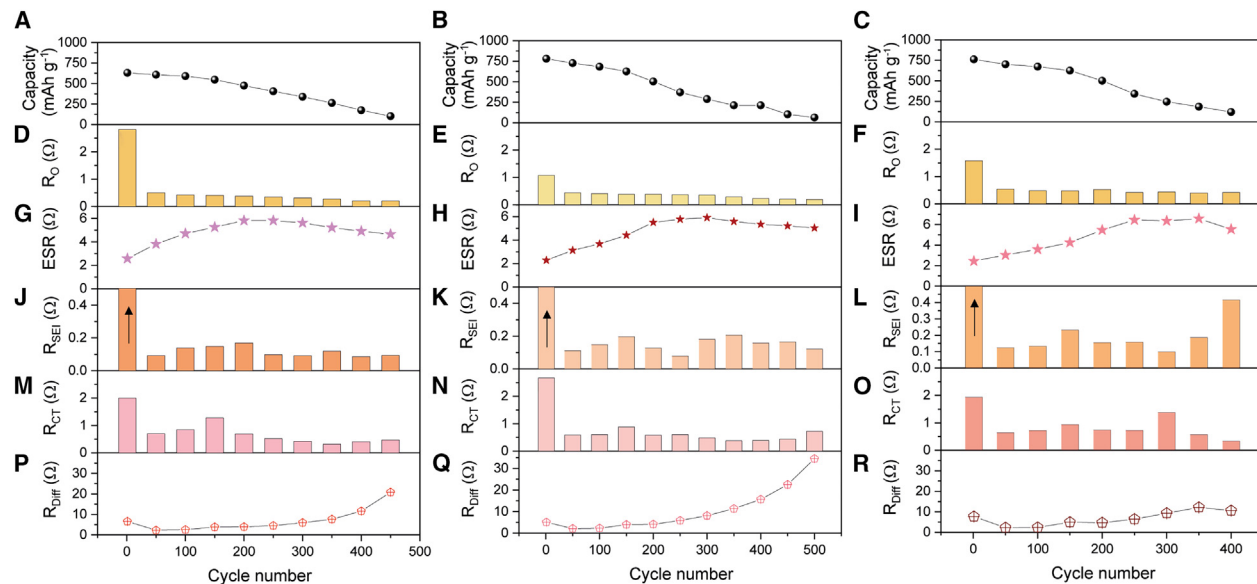


**Figure 5. Resistance values of different cell parameters extracted from DRT profiles during second-life analysis**

(A–C) Capacity values measured for cells 1, 2, and 3 at C/5.

(D–F)  $R_O$  values.

(G–I) ESR values.

(J–L)  $R_{SEI}$  values. Note that the  $R_{SEI}$  values measured after the formation cycle (cycle 0) were 11.23  $\Omega$  for cell 1, 5.92 for cell 2, and 21.74  $\Omega$  for cell 3; full datasets can be found in Figure S5.

(M–O)  $R_{CT}$  values.

(P–R)  $R_{Diff}$  values.

For values, see Tables S4–S6.

electrode interface, signifying the presence of a native oxide layer on the Li surface.<sup>8</sup> As with the data shown in Figure 1, the DRT profile changes during cycling are characterized by shifts in peak area and peak position (Figures 4B–4D and 4F, normalized distribution functions), signifying changes in the internal properties of the cell.

Cell capacity and different resistive components quantified from the DRT profiles of three cells as a function of cycle number are shown in Figure 5. The capacity of the three cells (Figures 5A–5C) fades consistently as the cell is cycled; however, the capacity fades at different rates at various stages of the cell cycling. Cell 1 retains 86% of the initial capacity after 150 cycles, whereas cells 2 and 3 retain 80% and 82%, respectively, during the same period, representing a rate of capacity fade in cell 1, cell 2, and cell 3 of 0.09%, 0.13%, and 0.12% per cycle, respectively. In cell 1, from 150 to 400 cycles, the capacity falls from 546 to 174  $\text{mAh g}^{-1}$ , a loss of 68% capacity (0.27% fade per cycle), whereas cell 2 lost 66% (0.26% fade per cycle), and cell 3 lost 80% (0.32% fade per cycle). These results indicate that Li-S cells capacity fade at a faster rate after the traditional defined end-of-life (20% loss in capacity); therefore, identifying and understanding the process causing this enhanced degradation is important to enhance the second-life viability of Li-S batteries. Various cell parameters extracted from the DRT profile of the three cells as a function of cycle number (plotted in Figure 5) were analyzed to identify processes responsible for capacity loss.

$R_O$  (Figures 5D–5F) calculated after the formation cycle (0 cycles) was 2.82, 1.07, and 1.57  $\Omega$  for cells 1, 2, and 3, decreasing to 0.50, 0.44, and 0.54  $\Omega$ , respectively, after 50 cycles. However, after 50 charge-discharge cycles, the  $R_O$  decreased more slowly, reaching 0.20, 0.23, and 0.42  $\Omega$ , respectively, for the 3 cells at the end of 400 cycles.

This decrease is likely caused by the gradual loss of S from within the positive electrode (S is melt infused in the pores of carbon), leaving a more conductive matrix structure. The observed change has little correlation with overall cell health and thus will be of little use in predicting cell failure.

A close look at the change in capacity of three cells (Figures 5A–5C) and ESR (Figures 5G–5I) with cycling reveals a clear link between ESR and capacity loss. ESR shows a linear increase with charge-discharge in the first 200 cycles consistent in 3 cells, increasing from 2.57 to 5.82 Ω in cell 1, 2.28 to 5.51 Ω in cell 2, and 2.43 to 5.47 Ω in cell 3, suggesting an increase in PS concentration in the electrolyte.<sup>11</sup> It is interesting that although ESR may be expected to continue to increase with further cycling, for cell 1 it reaches a maximum after 250 cycles (5.82 Ω), before showing a continuous decrease, reaching 4.91 Ω after 400 cycles. Similar trends were also observed in cells 2 and 3. As the Li-S cell is charged-discharged, the concentration of soluble PSs ( $\text{Li}_2\text{S}_{8.4}$ ) gradually increases in the electrolyte, reaching a maximum at the PS saturation concentration. Evidence for the reason behind the decrease in ESR after reaching maximum can be found in the progression of  $R_{\text{Diff}}$  (Figures 5P–5R);  $R_{\text{Diff}}$  increases with a very low rate up to the point of maximum ESR and afterward shows a large increase. For cell 1, the rate of  $R_{\text{Diff}}$  increase from 50 to 200 cycles is 0.011 Ω cycle<sup>-1</sup>, but jumps to 0.038 Ω cycle<sup>-1</sup> for the next 200 cycles ( $R_{\text{Diff}}$  cycle 50–200 = 0.013 Ω cycle<sup>-1</sup> and 0.016 Ω cycle<sup>-1</sup> for cells 2 and 3, then  $R_{\text{Diff}}$  cycle 200–400 = 0.057 and 0.374 Ω cycle<sup>-1</sup>). The diffusion resistance in the positive electrode is attributed to the precipitation of insulating  $\text{Li}_2\text{S}$  film in the positive electrode.<sup>24</sup> The ionic conductivity of the  $\text{Li}_2\text{S}$  is extremely low ( $\sim 10^{-13}$  S cm<sup>-1</sup>)<sup>25</sup>; therefore, the increase in  $R_{\text{Diff}}$  can be assigned to the buildup of  $\text{Li}_2\text{S}$  after end-of-life. The results show that the rate of formation of  $\text{Li}_2\text{S}$  increases when the electrolyte becomes saturated with PSs, with a simultaneous increase in capacity fade caused by the loss of active material.<sup>24</sup>

The change in the  $R_{\text{SEI}}$ , representing the resistance for Li-ion migration in the SEI, is significantly more dynamic than many of the other DRT peaks, showing a significant change in the region of cell life where the major capacity fading occurs. The evolution of  $R_{\text{SEI}}$  with cycling is given in Figures 5J–5L for cells 1, 2, and 3; the  $R_{\text{SEI}}$  values measured after the formation cycle were 11.23 Ω for cell 1, 5.92 for cell 2, and 21.74 Ω for cell 3 (Figure S5). We have shown in our previous report that this initial high  $R_{\text{SEI}}$  is associated with the presence of a native oxide/nitride layer on the fresh Li surface. After 50 charge-discharge cycles, the  $R_{\text{SEI}}$  decreased significantly to 0.09, 0.11, and 0.12 Ω for cells 1, 2, and 3, respectively, showing that the native film is removed after initial plating and stripping. In all three cells,  $R_{\text{SEI}}$  shows a continuous increase up to the point at which 20% of the initial capacity was lost (defined as end-of-life), but after this point, it decreases and shows unstable behavior. The positive electrode  $R_{\text{CT}}$  also showed similar complex behavior, increasing up to the cell traditionally defined end-of-life and fluctuating after this point, showing no clear trend. This is likely to be associated with complexity in the multiphase nature of positive electrode interphase in which carbon, S,  $\text{Li}_2\text{S}$ , binder, and PSs are undergoing rearrangements as the cell is cycled. The above analysis of different resistance components of cells indicates that after end-of-life, an increase in the rate of  $\text{Li}_2\text{S}$  precipitation in the positive electrode exacerbated by the saturation of electrolyte with PS along with the instability of the SEI are main contributors to the performance loss after end-of-life. Cell 3 suffered a short-circuit during charging after 397 cycles, which was evident from a sudden voltage decrease (Figure 3E); after this event, a drastic change was observed in the  $R_{\text{SEI}}$  value compared to other cell parameters, increasing by 2.3 times to 0.41. The significance of  $R_{\text{SEI}}$  values as a probable indicator of cell failure is explored later.

### Failure analysis of cells with commercial S electrodes

We also performed the analysis discussed above on commercial Nanomyte BE-70 electrodes ([Figure S6](#)) to validate the applicability of the DRT method on different positive electrode compositions. Figure S6A shows charge-discharge data of a Li-S cell fabricated with a Nanomyte electrode at C/5 until its failure; here, the cell undergoes charge-discharge for 535 cycles before it fails. The breaks in the continuity of the charge-discharge cycles ([Figure S6A](#)) represent the rest periods that were imposed before each impedance measurement to allow the cell to reach a steady state. [Figure S6B](#) shows the final charge-discharge cycles of this cell, in which it can be observed that short-circuiting begins to occur. As the cell was charged after the 535th cycle, the voltage dropped suddenly to  $\sim 0$  V ([Figure S6C](#)), but it then recovered to an open circuit voltage of 2.29 V, indicating the breaking of the short-circuit, which was likely driven by Li dendrites. However, when this cell was subjected to additional charge-discharge, it survived only a further 7 cycles before the voltage dropped to  $\sim 0$  V again ([Figure S6B](#)). Cell capacity variation with each cycle is shown in [Figure S6D](#); the cell capacity initially increased from 130 to 383 mAh g $^{-1}$  after 36 cycles, after which the cell showed relatively stable performance up to 150 cycles, with only an  $\sim 0.2$  mAh g $^{-1}$  loss per cycle. The capacity then fell rapidly up to 300 cycles, at which it again stabilized somewhat at  $\sim 150$  mAh g $^{-1}$ . Considering 383 mAh g $^{-1}$  as the maximum capacity, the cell reached 80% of this value after 148 cycles (184 cycles with respect to the beginning of cycling), which is similar to the end-of-life measured for lab-made cells. Reported Li-S cells usually show continuous capacity fade with each cycle; however, the Nanomyte electrodes used in this study commonly show activation in the initial cycles, likely due to the relatively heterogeneous-size S particles, followed by a regular capacity loss as the cell is cycled.<sup>8</sup>

DRT profiles of the Nanomyte-based cells calculated at 100% SoC are given in [Figure S7A](#), showing continuous evolution of cell internal properties. Note that the DRT profiles have the same number of peaks and the same characteristic features as the lab-made electrodes, albeit with slight differences in the magnitude of the polarization resistances. This consistency in peak patterns demonstrates that DRT analysis can be applied as a general diagnostic tool for Li-S cells. Major polarizations in the cell such as  $R_O$ ,  $R_{SEI}$ ,  $R_{CT}$ , and  $R_{Diff}$  show consistent change throughout the cycle life and therefore may be useful to track the cell SoH in this type of electrode ([Figures S7B–S7G](#), tabulated values in [Table S7](#)). The evolution of  $R_O$  during cycling is shown in [Figure S7C](#); after the formation cycle (0 cycles in [Figure S7C](#)),  $R_O$  is 1.16  $\Omega$ , and then it decreases to 0.68  $\Omega$  after 50 charge-discharge cycles, consistent with the growth and peak in cell capacity. This decrease in  $R_O$  can be attributed to the loss of S from the positive electrode because dissolved PS exposes more carbon in the process.<sup>8</sup> The  $R_O$ , however, remains stable up to 200 cycles and only changes significantly after  $\sim 350$  cycles, where it increases gradually up to 500 cycles, meaning that it shows little reflection of the most significant phase of capacity loss.

Continuous accumulation of insulating Li<sub>2</sub>S with time explains the trend in the evolution of  $R_O$ .<sup>13,26</sup> The trend in  $R_O$  is strikingly different from that observed in lab-made cells, where  $R_O$  shows a downward trend. The commercial electrodes are fabricated by mixing carbon black, sublimed S, and binder, whereas lab-made electrodes are fabricated from the melt-infused S-carbon composite, with S occupying pores in the carbon. Therefore, the nucleation properties of Li<sub>2</sub>S in the two cells is likely to be different, causing varied trends in the  $R_O$ .

The trend observed for ESR (Figure S7D) is consistent with that observed for lab-made cells. The initial increase in ESR is likely to be caused by the increased electrolyte viscosity, whereas at later stages, the increase in ESR can be assigned to the consumption of electrolytes at the negative electrode.<sup>27</sup>

The change in the  $R_{SEI}$  (Figure S7E) also shows dynamic behavior similar to the lab-made cells. Although the value is initially low due to the formation of SEI during first discharge (formation cycle), on subsequent analysis at 50 and 100 cycles, where cell capacity is at its peak, the  $R_{SEI}$  is very low: 0.10 and 0.21 Ω, respectively. An increase in resistance coincides with the commencement of capacity fade (cycle 150), and large increases occur as the cell capacity drops, plateauing close to cycle 300, as does the capacity. This behavior is consistent with the loss of electrolytes due to its reaction with the Li-metal negative electrode,<sup>28</sup> forming a thick layer at the interface as the cell is cycled.<sup>29</sup> Furthermore, polarization associated with  $R_{CT}$  of the cell (Figure S7F) also increases with cycling; as the cell is charge-discharged, electrochemically inactive Li<sub>2</sub>S precipitates at the carbon interface, blocking the reactive sites and resulting in high resistance for the electron transfer. Also,  $R_{Diff}$  shows a trend similar to cells 1 and 2, increasing very slowly in the end-of-life phase; however, it remains stable in the range of 4.3–4.27 Ω from 300 to 450 cycles and then increases rapidly to 8.82 and 18.68 Ω at the end of 500 and 550 cycles, respectively.

#### Role of $R_{SEI}$ in short-circuit prediction

In Figure S7E, a sudden decrease in  $R_{SEI}$  of the Nanomyte cell discussed above, from 2.51 to 1.77 Ω (30% decrease), after 450 cycles and an abrupt increase after 500 cycles can be observed. Drastic decreases and increases in the  $R_{SEI}$  may be indicative of the formation of soft-shorts (e.g., unstable dendrites); soft-shorts have previously been reported to occur in Li-ion and Zn-ion batteries.<sup>30</sup> Soft-shorts are different from full short-circuits because they do not cause the cell voltage to drop significantly, but they can cause self-discharge.<sup>30,31</sup> Shorting in the cell can also generate heat, causing faster degradation of the electrolyte, leading to the formation of a thick SEI layer, which may explain the increased  $R_{SEI}$  after 500 cycles<sup>28</sup> (Figure S7E). The formation of soft-shorts is usually reflected in the impedance spectra by a decrease in semicircle representing SEI charge transfer in the symmetric cells<sup>30</sup>; however, none of the impedance spectra of this cell measured after 400, 450, and 500 cycles (Figure S8) show a significant decrease in semicircle pointing to the complex situation in a Li-S full cell. As demonstrated, however, DRT is capable of identifying subtle changes in the  $R_{SEI}$ , making it a useful tool for cell diagnosis and failure prediction. As discussed above, cell 3, which was based on a lab-made electrode (Figure 5L), also showed an abrupt drastic increase in the  $R_{SEI}$  values measured at the point of short-circuit. The Nanomyte cell experienced a first hard short-circuit during the 536th cycle, leading to a voltage drop to 0.14 V, which was followed by a second short-circuit on cycle 542. A similar observation in the value of  $R_{SEI}$  was also noted in two more Nanomyte-based cells shown in Figure S9. Because short-circuits are mostly associated with negative electrode reactions, the changes in the  $R_{SEI}$  are highly likely to act as an indicator of cell failure via this common mode of degradation. A close look at the  $R_{SEI}$  values toward the end-of-life shows a huge increase in magnitude in the measurement immediately before the first short-circuit. A large value of  $R_{SEI}$  is indicative of a thick SEI layer that is more capable of short-circuiting than a thin SEI layer with dendrites. It is interesting that the  $R_{SEI}$  drops after the short-circuit (Figure S7E, after short circuit), which may be due to the current leak directly from the negative electrode to the positive electrode through the short-circuit.

## CONCLUSION

In this research, we have used DRT analysis to investigate the performance degradation of Li-S cells and identify distinctive features in the DRT profiles that can serve as predictive indicators for short-circuiting and cell failure. Our analysis encompassed cells containing both commercial (Nanomyte-based) and lab-made electrodes, allowing us to gain insights into the diagnostic capabilities of DRT for diverse Li-S cell configurations. Li-S cells operating at C/20 had a lifespan of only 65–100 cycles, whereas those operating at C/5 lasted for ~150 cycles. This performance decay during end-of-life was attributed to the instability of the Li SEI and the electrolyte decomposition at Li. In addition, beyond end-of-life, capacity decay was found to occur at a faster rate due to the increase in the rate of  $\text{Li}_2\text{S}$  precipitation at the positive electrode, which caused the loss of active material. Our findings consistently revealed that changes in the measured values of  $R_{SEI}$ , as obtained through DRT analysis, offer superior diagnostic capabilities for detecting cell failure. A significant increase in  $R_{SEI}$  was found to be indicative of imminent cell failure. Furthermore, we have detected the occurrence of soft-shorts in Li-S cells during both early and later cell life, which can have detrimental effects on cell performance. These observations provide opportunities to develop effective battery management solutions for Li-S batteries, enabling enhanced safety along with mechanisms to maximize cell performance and lifetime. Together, these developments can help propel Li-S batteries toward widespread commercial application. This method can also be applied to various Li-S chemistries,<sup>32</sup> Li-O<sub>2</sub> batteries,<sup>33</sup> and other metal battery systems.

## EXPERIMENTAL PROCEDURES

### Resource availability

#### Lead contact

Further information and requests for resources should be directed to and will be fulfilled by the lead contact, Thomas Miller ([t.miller@ucl.ac.uk](mailto:t.miller@ucl.ac.uk)).

#### Materials availability

This study did not generate new unique materials.

#### Data and code availability

The data presented in this work are available from the corresponding authors upon reasonable request. This study did not generate any code.

### Materials

Nanomyte BE-70 S positive electrodes were procured from the NEI Corporation. The electrodes, composed of 70 wt % S, 10 wt % polyvinylidene fluoride (PVDF) binder and 20 wt % carbon black, were used as received. The active loading of S was 3.4 mg cm<sup>-2</sup> (thickness 55  $\mu\text{m}$ ). S, PVDF, and Cyrene (dihydrolevoglucosanone) were procured from Sigma-Aldrich, whereas Timcal Super C65 and Li disks (15.6 mm diameter and 0.45 mm thickness) were purchased from PI-KEM. For electrolyte preparation, 1,2-dimethoxyethane (DME), 1,3-dioxolane (DOL) solvents, Li bis(trifluoromethanesulfonyl)imide (LiTFSI), and LiNO<sub>3</sub> salts were provided by Sigma-Aldrich. AvCarb P50 carbon paper was purchased from Fuel Cell Store.

### Electrode preparation

For electrode fabrication, Cyrene was used as a solvent. Carbon and S were mixed with a mortar and pestle in a 77:23 ratio, which was then heated in a Teflon-lined autoclave at 155°C for 4 h for melt infusion of S inside the carbon pores. This S-carbon composite (90 wt %) and PVDF (10 wt %) were then mixed via ball milling

(300 rpm for 1 h); the total solid content in the slurry was kept at 17%. The final composition in the electrodes was 70 wt % S, 20 wt % carbon, and 10 wt % PVDF. The slurry was then drop coated on a carbon (AvCarb P50) current collector (14 mm disk), which was then dried on a hot plate at 50°C for 6 h in ambient air. Before cell fabrication, the electrodes were dried in a vacuum oven at 40°C for 12 h. S loading on the lab-made electrodes was between 3 and 3.5 mg/cm<sup>2</sup>.

### Electrochemical measurements

All of the electrochemical measurements were performed on a VSP Biologic multi-channel potentiostat at room temperature. EIS measurements were performed under open-circuit conditions with an amplitude of 5 mV; measurements were made by scanning the frequency from 1 MHz to 50 mHz (swept from high to low frequency) and recording 10 points per decade for each EIS measurement. Cells were rested for 2 h postfabrication to allow electrode wetting. Formation cycles were performed by first discharging the cell to 1.8 V at C/20 ( $C = 1,675 \text{ mA g}^{-1}$ ), followed by a full charge-discharge cycle at C/20 in the voltage range of 1.8–2.6 V. The cells were kept at OCV for 5 h to allow the cell to achieve steady state before EIS measurements were made.

### Cell fabrication

Two-electrode CR2032 coin cells were constructed by stacking a Li disk (0.45 mm thick, 15.6 mm diameter, 2,072% excess Li in cell), a separator (Celgard-2400, 25 µm), and an S<sup>+</sup> electrode, before an electrolyte containing 1 M LiTFSI and 0.25 M LiNO<sub>3</sub> (1 M LiNO<sub>3</sub> in Nanomyte cells) in a 1:1 v/v mixture of DOL/DME was added. Two 0.5 mm spacers and a spring (1.2 mm high and 0.3 mm thick) were used in the cell. An electrolyte-to-S ratio of 15 µL/mg<sub>Sulfur</sub> was used in all of the cells.

### DRT analysis

To conduct the DRT analyses, an open-source MATLAB script-based software (DRT Tools) was used. The Tikhonov regularization was used to fit discrete experimental data in a nonlinear least-squares manner with the Gaussian method for data discretization. Both real and imaginary components of the EIS were used to fit the experimental data, with inductive data discarded. Second-order regularization derivative fitting parameters were used, and the regularization parameter was set at  $1 \times 10^{-4}$  (residuals between real impedance and impedance derived from DRT are acceptably low for this value), and the radial basis function with a full width at half-maximum (FWHM) of 0.5 was used; these parameters resulted in an appropriate fitting of the EIS data. DRT spectra were fitted with a Gaussian nonlinear curve using the Levenberg-Marquardt iteration method in Origin to calculate the polarization resistance and time constants. For peak fitting, the number of peaks was manually selected, with the specific allocation discussed later and elsewhere,<sup>8</sup> and the base of the peak was fixed to zero, whereas other peak parameters such as position, area, and FWHM were not fixed, and the iterations were performed until the convergence of fit (to reach  $R^2 \sim 1$ ).

## SUPPLEMENTAL INFORMATION

Supplemental information can be found online at <https://doi.org/10.1016/j.xcsp.2024.101833>.

## ACKNOWLEDGMENTS

This work was supported by the Faraday Institution ([www.faraday.ac.uk](http://www.faraday.ac.uk); EP/S003053/1) through the Lithium Sulfur Technology Accelerator (LiSTAR) program (FIRG014, FIRG058).

## AUTHOR CONTRIBUTIONS

Electrode preparation and coin cell fabrication was carried out by R.S. and J.H. J.B.R. participated in technical discussions. Experiment design, data collection, and analysis was performed by R.S. R.S., A.J.E.R., and T.S.M. drafted and edited the manuscript. This project was supervised by T.S.M.

## DECLARATION OF INTERESTS

The authors declare no competing interests.

Received: July 27, 2023

Revised: December 22, 2023

Accepted: January 24, 2024

Published: February 14, 2024

## REFERENCES

1. Robinson, J.B., Xi, K., Kumar, R.V., Ferrari, A.C., Au, H., Titirici, M.-M., Parra-Puerto, A., Kucernak, A., Fitch, S.D.S., Garcia-Araez, N., et al. (2021). 2021 roadmap on lithium sulfur batteries. *JPhys Energy* 3, 031501. <https://doi.org/10.1088/2515-7655/abdb9a>.
2. Mistry, A.N., and Mukherjee, P.P. (2018). "Shuttle" in polysulfide shuttle: friend or foe? *J. Phys. Chem. C* 122, 23845–23851. <https://doi.org/10.1021/acs.jpcc.8b06077>.
3. Knap, V., Auger, D., Propp, K., Fotouhi, A., and Stroe, D.I. (2018). Concurrent real-time estimation of state of health and maximum available power in lithium-sulfur batteries. *Energies* 11, 2133. <https://doi.org/10.3390/en11082133>.
4. Shahriari, M., and Farrokhi, M. (2013). Online state-of-health estimation of VRLA batteries using state of charge. *IEEE Trans. Ind. Electron.* 60, 191–202. <https://doi.org/10.1109/TIE.2012.2186771>.
5. Coleman, M., Lee, C.K., Zhu, C., and Hurley, W.G. (2007). State-of-charge determination from EMF voltage estimation: using impedance, terminal voltage, and current for lead-acid and lithium-ion batteries. *IEEE Trans. Ind. Electron.* 54, 2550–2557. <https://doi.org/10.1109/TIE.2007.899926>.
6. Galeotti, M., Giannanco, C., Cinà, L., Cordiner, S., and Di Carlo, A. (2015). Synthetic methods for the evaluation of the State of Health (SOH) of nickel-metal hydride (NiMH) batteries. *Energy Convers. Manag.* 92, 1–9. <https://doi.org/10.1016/j.enconman.2014.12.040>.
7. Propp, K., Auger, D.J., Fotouhi, A., Marinescu, M., Knap, V., and Longo, S. (2019). Improved state of charge estimation for lithium-sulfur batteries. *J. Energy Storage* 26, 100943. <https://doi.org/10.1016/j.est.2019.100943>.
8. Soni, R., Robinson, J.B., Shearing, P.R., Brett, D.J., Rettie, A.J., and Miller, T.S. (2022). Lithium-sulfur battery diagnostics through distribution of relaxation times analysis. *Energy Storage Mater.* 51, 97–107. <https://doi.org/10.1016/j.ensm.2022.06.016>.
9. Chen, J., Quattrocchi, E., Ciucci, F., and Chen, Y. (2023). Charging processes in lithium-oxygen batteries unraveled through the lens of the distribution of relaxation times. *Chem* 9, 2267–2281. <https://doi.org/10.1016/j.chempr.2023.04.022>.
10. Noh, H., Song, J., Park, J.K., and Kim, H.T. (2015). A new insight on capacity fading of lithium-sulfur batteries: The effect of Li<sub>2</sub>S phase structure. *J. Power Sources* 293, 329–335. <https://doi.org/10.1016/j.jpowsour.2015.05.072>.
11. Yan, J., Liu, X., and Li, B. (2016). Capacity fade analysis of sulfur cathodes in lithium–sulfur batteries. *Adv. Sci.* 3, 1600101. <https://doi.org/10.1002/advs.201600101>.
12. Risse, S., Cañas, N.A., Wagner, N., Härk, E., Ballauff, M., and Friedrich, K.A. (2016). Correlation of capacity fading processes and electrochemical impedance spectra in lithium/sulfur cells. *J. Power Sources* 323, 107–114. <https://doi.org/10.1016/j.jpowsour.2016.05.032>.
13. Marinescu, M., O'Neill, L., Zhang, T., Walus, S., Wilson, T.E., and Offer, G.J. (2018). Irreversible vs reversible capacity fade of lithium-sulfur batteries during cycling: The effects of precipitation and shuttle. *J. Electrochem. Soc.* 165, A6107–A6118. <https://doi.org/10.1149/2.0171801jes>.
14. Casals, L.C., Amante García, B., and Canal, C. (2019). Second life batteries lifespan: rest of useful life and environmental analysis. *J. Environ. Manag.* 232, 354–363. <https://doi.org/10.1016/j.jenvman.2018.11.046>.
15. Danzer, M.A. (2019). Generalized distribution of relaxation times analysis for the characterization of impedance spectra. *Batteries* 5, 53. <https://doi.org/10.3390/batteries5030053>.
16. Zheng, J., Lv, D., Gu, M., Wang, C., Zhang, J.G., Liu, J., and Xiao, J. (2013). How to obtain reproducible results for lithium sulfur batteries? *J. Electrochem. Soc.* 160, A2288–A2292. <https://doi.org/10.1149/2.106311jes>.
17. Zhang, S. (2012). Improved cyclability of liquid electrolyte lithium/sulfur batteries by optimizing electrolyte/sulfur ratio. *Energies* 5, 5190–5197. <https://doi.org/10.3390/en5125190>.
18. Zhou, G., Pei, S., Li, L., Wang, D.W., Wang, S., Huang, K., Yin, L.C., Li, F., and Cheng, H.M. (2014). A graphene–pure-sulfur sandwich structure for ultrafast, long-life lithium–sulfur batteries. *Adv. Mater.* 26, 625–664. <https://doi.org/10.1002/adma.201302877>.
19. Zhou, L., Danilov, D.L., Eichel, R., and Notten, P.H.L. (2021). Host materials anchoring polysulfides in Li-S batteries reviewed. *Adv. Energy Mater.* 11, 2001304. <https://doi.org/10.1002/aenm.202001304>.
20. Dörfler, S., Althues, H., Härtel, P., Abendroth, T., Schumm, B., and Kaskel, S. (2020). Challenges and key parameters of lithium-sulfur batteries on pouch cell level. *Joule* 4, 539–554. <https://doi.org/10.1016/j.joule.2020.02.006>.
21. Wang, W., Zhang, J., Chou, J., Yin, Y., You, Y., Xin, S., and Guo, Y. (2021). Solidifying cathode–electrolyte interface for lithium–sulfur batteries. *Adv. Energy Mater.* 11, 2000791. <https://doi.org/10.1002/aenm.202000791>.
22. Wolff, D., Canals Casals, L., Benveniste, G., Corchero, C., and Trilla, L. (2019). The effects of lithium sulfur battery ageing on second-life possibilities and environmental life cycle assessment studies. *Energies* 12, 2440. <https://doi.org/10.3390/en12122440>.
23. Park, M., Zhang, X., Chung, M., Less, G.B., and Sastry, A.M. (2010). A review of conduction phenomena in Li-ion batteries. *J. Power Sources* 195, 7904–7929. <https://doi.org/10.1016/j.jpowsour.2010.06.060>.
24. Zhang, T., Marinescu, M., Walus, S., and Offer, G.J. (2016). Modelling transport-limited discharge capacity of lithium-sulfur cells. *Electrochim. Acta* 219, 502–508. <https://doi.org/10.1016/j.electacta.2016.10.032>.
25. Ye, H., Li, M., Liu, T., Li, Y., and Lu, J. (2020). Activating Li<sub>2</sub>S as the lithium-containing cathode in lithium–sulfur batteries. *ACS Energy Lett.* 5, 2234–2245. <https://doi.org/10.1021/acsenergylett.0c00936>.
26. Fan, F.Y., Carter, W.C., and Chiang, Y.-M. (2015). Mechanism and kinetics of Li<sub>2</sub>S

- precipitation in lithium–sulfur batteries. *Adv. Mater.* 27, 5203–5209. <https://doi.org/10.1002/adma.201501559>.
27. Boenke, T., Kirchhoff, S., Reuter, F.S., Schmidt, F., Weller, C., Dörfler, S., Schwedtmann, K., Härtel, P., Abendroth, T., Althues, H., et al. (2022). The role of polysulfide-saturation in electrolytes for high power applications of real world Li–S pouch cells. *Nano Res.* 16, 8313–8320. <https://doi.org/10.1007/s12274-022-5017-8>.
28. Liu, J., Bao, Z., Cui, Y., Dufek, E.J., Goodenough, J.B., Khalifah, P., Li, Q., Liaw, B.Y., Liu, P., Manthiram, A., et al. (2019). Pathways for practical high-energy long-cycling lithium metal batteries. *Nat. Energy* 4, 180–186. <https://doi.org/10.1038/s41560-019-0338-x>.
29. Heiskanen, S.K., Kim, J., and Lucht, B.L. (2019). Generation and evolution of the solid electrolyte interphase of lithium-ion batteries. *Joule* 3, 2322–2333. <https://doi.org/10.1016/j.joule.2019.08.018>.
30. Li, Q., Chen, A., Wang, D., Pei, Z., and Zhi, C. (2022). “Soft Shorts” hidden in zinc metal anode research. *Joule* 6, 273–279. <https://doi.org/10.1016/j.joule.2021.12.009>.
31. Zhang, X., Sahraei, E., and Wang, K. (2016). Li-ion battery separators, mechanical integrity and failure mechanisms leading to soft and hard internal shorts. *Sci. Rep.* 6, 32578. <https://doi.org/10.1038/srep32578>.
32. Song, Z., Zhang, T., Liu, S., Shao, W., Jiang, W., Mao, R., Jian, X., and Hu, F. (2023). Sulfur polymerization strategy based on the intrinsic properties of polymers for advanced binder-free and high-sulfur-content Li–S batteries. *SusMat* 3, 111–127. <https://doi.org/10.1002/sus.2110>.
33. Ren, Y., Fan, J.S., and Fu, Y.z. (2023). Recent strategies for improving the performances of rechargeable lithium batteries with sulfur- and oxygen-based conversion cathodes. *Energy Mater.* 3, 300015. <https://doi.org/10.20517/energymater.2022.78>.